Available online at www.sciencedirect.com
SCIENCE DIRECT®
Journal of Chromatography A, 1006 (2003) 207–228
JOURNAL OF CHROMATOGRAPHY A
www.elsevier.com/locate/chroma

Chromatographic performance of monolithic and particulate stationary phases
Hydrodynamics and adsorption capacity

Felix C. Leinweber, Ulrich Tallarek*
Institut für Verfahrenstechnik, Otto-von-Guericke-Universität Magdeburg, Universitätsplatz 2, D-39106 Magdeburg, Germany

Abstract

Monolithic chromatographic support structures offer, as compared to the conventional particulate materials, a unique combination of high bed permeability, optimized solute transport to and from the active surface sites and a high loading capacity by the introduction of hierarchical order in the interconnected pore network and the possibility to independently manipulate the contributing sets of pores. While basic principles governing flow resistance, axial dispersion and adsorption capacity are remaining identical, and a similarity to particulate systems can be well recognized on that basis, a direct comparison of sphere geometry with monolithic structures is less obvious due, not least, to the complex shape of the skeleton domain. We present here a simple, widely applicable, phenomenological approach for treating single-phase incompressible flow through structures having a continuous, rigid solid phase. It relies on the determination of equivalent particle (sphere) dimensions which characterize the corresponding behaviour in a particulate, i.e. discontinuous bed. Equivalence is then obtained by dimensionless scaling of macroscopic fluid dynamical behaviour, hydraulic permeability and hydrodynamic dispersion in both types of materials, without needing a direct geometrical translation of their constituent units. Differences in adsorption capacity between particulate and monolithic stationary phases show that the silica-based monoliths with a bimodal pore size distribution provide, due to the high total porosity of the material of more than 90%, comparable maximum loading capacities with respect to random-close packings of completely porous spheres.

Keywords: Monolithic columns; Stationary phases, LC; Hydrodynamic; Adsorption; Packed columns; Permeability; Dispersion

1. Introduction

Monolithic high surface area materials have found a number of applications in industrial and environmental technologies, e.g. as ceramic supports for high-temperature heterogeneous solid-phase–gas phase catalysis (especially as automotive exhaust gas catalysts and in industrial gas purification), as condensators, and in liquid chromatography [1–7]. Due to the reduced dynamic viscosity of gases at elevated temperatures, solid-phase catalysts for gas reactions usually are highly ordered microporous media with a monomodal pore size distribution. Stationary phases for liquid chromatography, however, preferably have a hierarchically-structured pore space with macropores dedicated for convective mass transport through the column and mesopores inside the (itself

*Corresponding author. Tel.: +49-391-611-0465; fax: +49-391-671-2028.
E-mail address: ulrich.tallarek@vst.uni-magdeburg.de (U. Tallarek).

0021-9673/03/$ – see front matter
doi:10.1016/S0021-9673(03)00391-1

porous) support material. This offers a large surface area accessible via diffusion-limited mass transfer. Such bimodal pore size distributions can be realized by packing micrometre-sized mesoporous particles into the desired column geometry. A reduced axial dispersion, one of the goals in high-performance liquid chromatography, is accomplished when the large and irregularly shaped particles first used in (low-pressure) liquid chromatography are replaced by spheres of only a few micrometres in diameter with a narrow size distribution (Fig. 1), because dispersion associated with the liquid hold-up (intraparticle stagnant mobile phase mass transfer resistance) can be then significantly reduced due to a decreased characteristic diffusion path length in the stagnant zone [8]. Additionally, mechanical dispersion may be reduced by an increased packing homogeneity due to a uniform particle shape [9]. Although hydrodynamic dispersion analysis suggests the use of spheres as small as possible, any further reduction of particle size to the submicrometre range is of only limited value because the resulting beds create an unacceptably high back pressure [10] and, further, slurry packing of these columns is impeded by problems in getting the submicron spheres settled reasonably into a ''fixed'' bed [11].

Another aspect concerning the hydrodynamics in a random-close packing of completely porous spheres is that the mean interparticle macropore diameter (affecting the hydraulic permeability) and particle or domain size (influencing axial dispersion) cannot be manipulated independently as both parameters are ultimately coupled with the mean particle diameter. Pellicular [12] and nonporous particles [13,14] may be an alternative but lack a large effective surface area. In order to overcome these limitations for a fixed bed of spheres with its particulate (and, therefore, discontinuous) solid-phase, monolithic structures can be a solution because, in their continuous solid-phase, the macropore diameter and domain size can be adjusted independently over the complete length of the bed. Monolithic media for liquid chromatography can be distributed into two main categories based on their manufacturing material: organic polymer [15–20] and silica-based monoliths [21–26]. The macroscopic differences in bed morphology are revealed by SEM pictures of some of the commercially available monolithic stationary phases

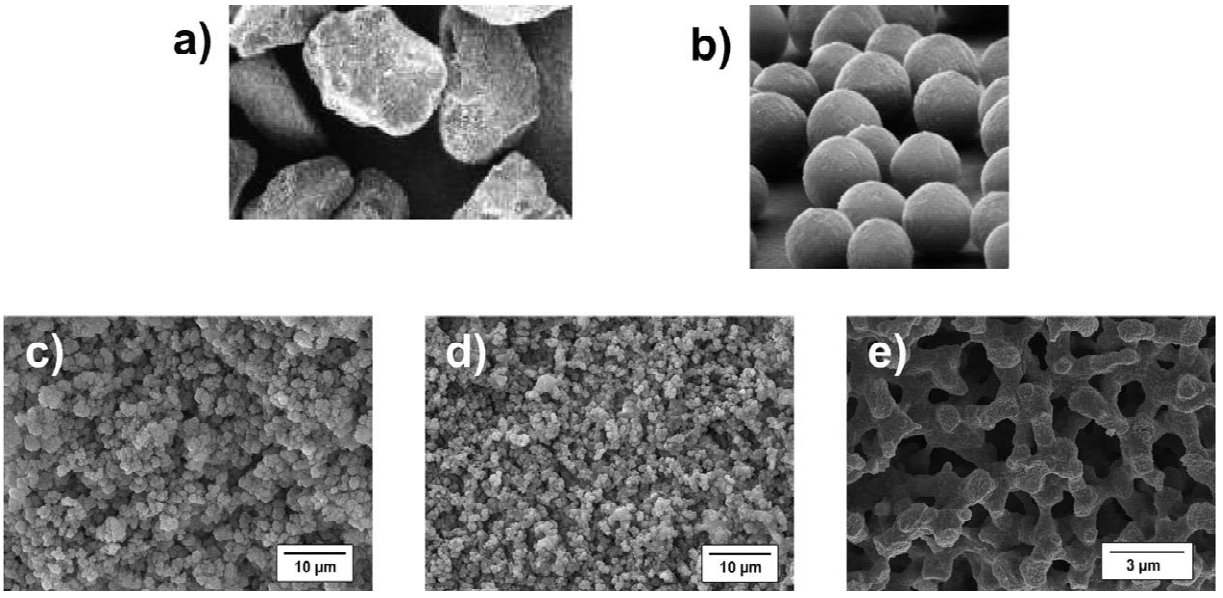

Fig. 1. Scanning electron microscopy pictures of different types of porous chromatographic materials. (a) Irregularly-shaped silica particles, (b) spherical silica particles, (c) organic polymer monolith A (UNO S), (d) organic polymer monolith B (CIM Disk), and (e) silica-based monolith (Chromolith).

(Fig. 1). Since the bed structure of organic polymer monoliths more or less resembles that of a loose packing of spherical or nearly so particles (microglobules) with a broad size distribution, the silica monoliths show a more fractal morphology with large interskeleton pore space. Differences in macroscopic stationary phase structures are intensified by the pore size distribution measurements (Fig. 2, although these measurements do not contain information about the actual pore interconnectivity) and these can be, by referring to the original literature, directly related to the respective preparation process: the organic polymer monoliths are synthesized by a thermally initiated one-step radical polymerization process in the presence of a mixture of porogens that induces phase separation and creates the interskeleton macropores [5]. The reaction temperature and composition of the porogenic mixture determine the macropore, as well as the microglobule diameter, but both also influence the development of micropores in the microglobules, hence in the stationary phase, so that reaction conditions are normally adjusted to lead to a nearly nonporous skeleton and, for sufficiently large molecules, to an effectively monomodal pore size distribution [27]. Silica-based monoliths, in contrast, are prepared through a two-step process involving a sol–gel mechanism overlapped by a spinodal phase transition process as the first step (this determines domain size and macropore diameter), followed by a solvent exchange as the second one, leaching out the silica skeleton to create the intraskeleton mesopore space [28–32]. Consequently, the resulting pore space shows a bimodal pore size distribution [21]. Up to date, only the use of silica as the basis material for monoliths in chromatography allows to create a hierarchically-structured pore space with independent adjustment of all skeleton parameters. Based on preparation aspects, most of the applications for polymer monoliths are in the purification (downstreaming) process of biomacromolecules like proteins and plasmid-DNA [33–35], while the silica-based monoliths as stationary phase material in partitioning chromatography are mainly used for low- and medium molecular mass substances [36–38].

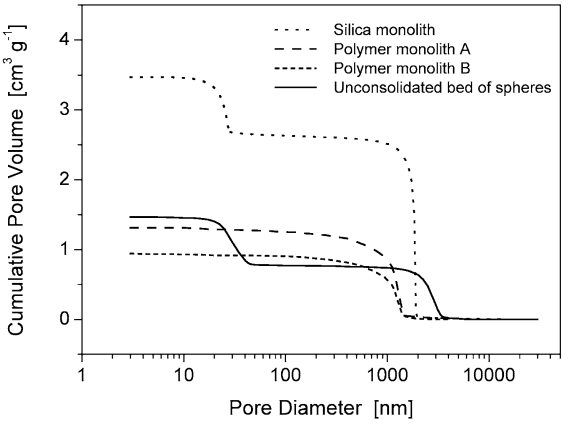

Fig. 2. Cumulative pore volume data for the monolithic and particulate fixed beds indicating monomodal pore size distributions in the case of the polymer monoliths and bimodal pore size distributions for both the silica-based monolith and the bed of porous silica beads.

Polymeric continuous stationary phases for liquid chromatography offer, in comparison with the particulate fixed beds, the possibility to be easily prepared in any dimension desired, in normal tube [15] and in disk format [19], and in radial flow geometry [39] or on microfluidic devices [40,41], whereas for silica-based materials the column geometry has to be fitted to the stationary phase due to the syneresis of the silica-gel [21,32]. One main restriction for both polymeric and silica-based monolithic structures is, since the stationary phase cannot be packed under a high pressure into the confining column geometry, the proper attachment of the stationary phases to the column wall. This results in a maximum operating pressure (recommendation) ranging from 1 to 5 MPa for the organic polymers and up to 20 MPa for the silica monoliths. Another problem concerning highly permeable monolithic structures or those in an extraordinary geometry like a disk or radial flow type is the proper (radial) sample introduction. In comparison to packed beds of small particles in narrow-diameter columns, there exists no sufficiently high back pressure to create a more homogeneous radial flow distribution [42]. Further, polymeric monolithic stationary phases are, like the conventional polymer beads, restricted to an eluent composition prohibiting the use of strong organic solvents due to swelling of the skeleton [5].

In any confining geometry the description of the respective flow regime via Reynolds and Peclet numbers relies on the definition of some characteris-

tic and, over the length of the bed, constant dimension $\mathscr{L}$ of the respective medium [10,43]. In open-tubular geometry this dimension is the inner column diameter, while for a fixed bed of (completely) porous spheres the mean particle diameter is a good measure for the determination of Reynolds and Peclet numbers (Fig. 3). In the monolithic structures there also exists a continuously repeating geometrical unit, for the silica monoliths it is the average domain size [22,26], or for polymer monoliths the mean microglobule diameter [27]. However, monolithic resins are not closely packed and they rather provide a large interskeleton porosity impeding the direct use of some characteristic geometrical skeleton units to determine a particular flow regime. The hydraulic permeability is certainly a function of interstitial porosity, macropore diameter, and domain size (as well as of their distribution functions). Axial dispersion depends on the size and porosity of the domain, on the macropore diameter and the pore (inter)connectivity. The consideration of permeability functions similar to those established for random-close packings of spheres [44–46] may actually fail because pore space morphology of each monolith offers unique geometrical properties and the differences between monoliths cannot, in contrast to that for fixed beds of nearly spherical particles, be easily reduced to only a few macroscopically relevant bed parameters. To obtain insight into the hydrodynamic behaviour of the various monolithic stationary phases it is, thus, favourable not to try to set up a model for a particular monolithic system, but to rather scale their hydrodynamic behaviour to that of the (well established) systems of particulate fixed beds via introduction of ''equivalent sphere dimensions'' for permeability and dispersion in monoliths, in general [47,48]. By defining $\mathscr{L}_{flow}$ and $\mathscr{L}_{disp}$ (Fig. 3 [48]) for hydrodynamics in different monoliths their behaviour

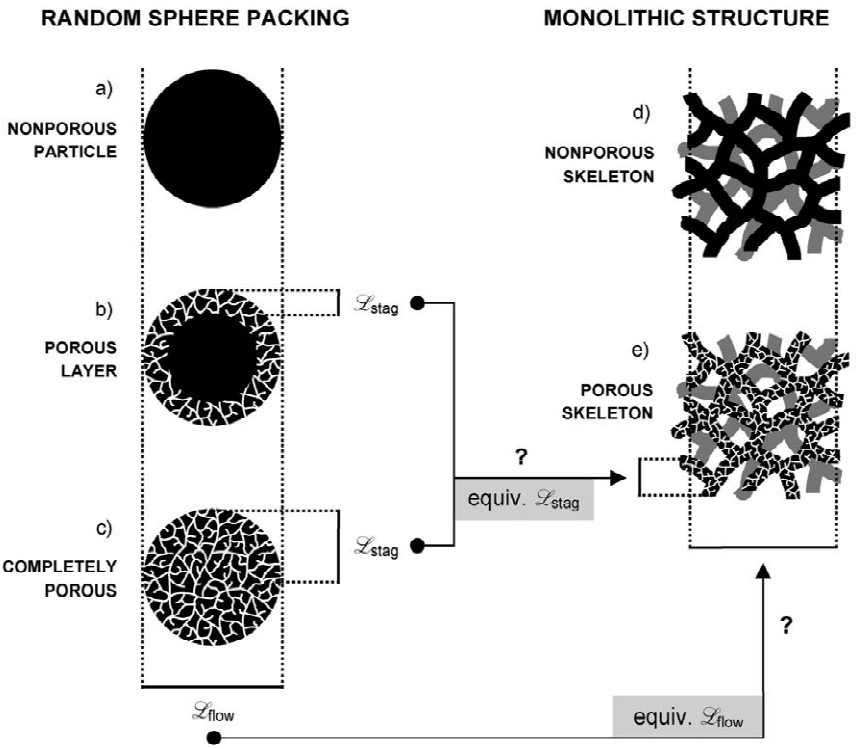

Fig. 3. Characteristic length-scales for hydraulic permeability and hydrodynamic dispersion in a bed of spheres and in monoliths. While the particle diameter is useful to define a region impermeable for flow, the actual thickness of the porous layer may be used to address the dispersion originating in stagnant zones of a sphere packing. Apparently $\mathscr{L}_{stag}$ and $\mathscr{L}_{flow}$ are different. Adapted with permission from Tallarek et al. [48].

is translated into the diameter and porosity of a spherical particle in a fixed bed of such spheres which shows an identical macroscopic flow resistance and/or the identical longitudinal dispersion characteristics.

The purpose of our current investigation is to analyze the hydrodynamics of monolithic stationary phase materials in comparison to some particulate reference materials. The general (and widely applicable) phenomenological approach of dimension analysis allows the scaling of permeability and dispersivity data from particulate media and from both polymer and silica-based monoliths. The hydrodynamic analysis is complemented by adsorption capacity studies for the silica-based materials covering RP4e, RP8e and RP18e surface modification. The monolithic and particulate chromatographic media are quantitatively compared via three main chromatographically relevant parameters: pressure drop, efficiency and adsorption capacity.

2. Experimental

2.1. Chemicals

Acetone, caffeine, trifluoroacetic acid (TFA), and acetonitrile (gradient grade) were purchased from Merck (Darmstadt, Germany). Purified water was prepared on a Milli-Q water purification system. Angiotensin II, insulin and bovine serum albumin (BSA) were purchased from Sigma.

2.2. Columns

Silica-based monoliths (Chromolith Performance RP18e) with mean intraskeleton mesopores of 25 nm, as well as a column of LiChrospher WP300 RP18e spheres having 30 nm mesopores were obtained from Merck. A Zorbax SB300-C_{18} column was obtained from Agilent Technologies (Waldbronn, Germany), a Micra NPS column packed with nonporous particles was purchased from Bischoff Analysentechnik (Leonberg, Germany). The particle size distribution functions of all particulate porous media were measured after the completion of experiments on a CILAS 968 laser light diffraction and diffusion system (CILAS, Marcoussis, France). An integration of each population distribution led to the mean surface-averaged particle diameter ($\bar{d}_{p,2}$). Polymer-based monoliths CIM Disk SO_3 and UNO S Polishing Kit were purchased from BiaSeparation (Lubljana, Slovenia) and from Bio-Rad (Munich, Germany). The pore size distributions and specific surface area data of all porous materials were determined by mercury intrusion and nitrogen adsorption at Merck. Scanning electron microscopy pictures were taken at the Mikrostrukturzentrum of the Otto-von-Guericke-Universität Magdeburg. A comprehensive overview of the properties of different fixed beds used in the permeability and dispersion analysis is given in Table 1.

Chromolith Performance monolithic columns (100×4.6 mm) with an RP4e, RP8e and RP18e surface modification containing 12.5 nm mesopores and macropores of 1.9 μm were obtained from Merck. PurospherSTAR RP18e in a particulate reference column (55×4.0 mm) for the adsorption capacity studies (3 μm particle diameter and 12 nm mesopore diameter) was also obtained from Merck.

2.3. Apparatus

All measurements on hydraulic permeability, van Deemter curves and adsorption capacity were conducted on a Merck–Hitachi HPLC system. Each column material was first thoroughly wetted with pure acetonitrile (except organic polymer monoliths) and, thereafter, the total pressure drop was recorded with purified, degassed water until the maximum possible flow-rate was reached. Correction by the system back pressure gave the column pressure drop. All dispersion experiments were conducted on an Agilent 1100 capillary HPLC system including a binary low-pressure gradient pump, an autosampler, and UV detector. The microlitre flow control sensor was bypassed and the eluent was directly delivered in isocratic mode in the range from 100 to 2500 μl/min by the pump. The volumetric flow-rate through each column was determined by measuring elution volume over time behind the detection cell. The actual flow-rate deviated within 2% of the system value. All connecting tubes were replaced by 200 μm I.D. capillary tubing from Agilent with a maximum length of 10 cm between injection valve and column, both to avoid a high system pressure-

Table 1
Characteristic dimensions and parameters of porous media used in this study

Fixed bed[a]	L_{bed} (mm)	d_{col} (mm)	V_{extra}/V_{bed} [b]	$\bar{d}_{p,2}$ (μm)	d_{macro} (μm)	ρ_{bed} (g/ml)	ε_{total}	ε_{inter}	ε_{intra}	τ_{intra}	Φ	A_{spec} (m^2/g)	A_{rel} (m^2/ml)
Nonporous spheres	53	4.6	0.02	3.2	–	1.20	0.36	0.36	–	–	1.78	1	1
Porous spheres A	50	2.1	0.10	4.3	–	0.87	0.65	0.37	0.44	1.28	0.54	51	44
Porous spheres B	55	2.0	0.10	7.2	–	0.85	0.75	0.37	0.60	1.20	0.33	76	65
Silica monolith	100	4.6	0.01	–	1.9	0.26	0.92	0.72	0.70	1.15	0.09	147	39
Polymer monolith A	10	4.6	0.10	–	1.1	0.76	0.70	0.70	–	–	0.43	4.4	3.3
Polymer monolith B	3	12	0.42	–	1.1	1.06	0.47	0.47	–	–	1.13	3.6	3.8

[a] Nonporous spheres, Micra NPS; porous sphere packing A, Agilent Zorbax SB300-C_{18}; porous sphere packing B, Merck LiChrospher WP300 RP18e; silica monolith, Merck Chromolith; polymer monolith A, BioRad UNO S Polishing Kit; polymer monolith B, BiaSeparations CIM Disk SO_3.

[b] $V_{extra} = 17$ μl, except with polymer monolith B for which $V_{extra} = 142$ μl (resulting from the disk housing).

drop at maximum flow-rates and to minimize extra-column volume. The column was directly connected to a 5 μl semi-micro detection cell. Data acquisition rate was increased up to 50 Hz at highest volumetric flow-rates to prevent artificial band broadening due to an insufficient detector response time.

2.4. Elution conditions

Dispersion analysis under non-retained elution conditions was achieved for all tracers by the use of premixed eluents consisting of a water–acetontrile (50:50) mixture, adjusted to acidic conditions for reversed-phase materials by addition of 0.1% (v/v) trifluoroacetic acid and to basic conditions for the strong cation-exchange polymer monoliths with 10 m*M* sodium phosphate buffer (pH 11). Prior to use, the eluents were filtered with 0.45 μm membrane filters and degassed with helium. The injection volume ranged between 1 and 5 μl (depending on the bed volume) with sample concentrations of 0.5% (v/v) for acetone, 20 μg/ml for angiotensin II and 50 μg/ml for insulin and BSA. Each sample was dissolved in the mobile phase to avoid concentration effects due to different elution strengths. Detection was carried out at 215 nm (ref.: 250 nm) with 10 nm bandwidth, except for acetone (254 nm, ref.: 330 nm). Elution was made at controlled room temperature (21 °C).

Van Deemter curves for caffeine were recorded at increasing flow-rate in two independent runs. The retention factor was adjusted to $k' = 5$ for all stationary phase materials yielding in eluent compositions of water–acetonitrile of 92:8, 94:6, 94.5:5.5 and 95:5 for the RP18e particles, the RP18e, RP8e and RP4e silica monolith, respectively. All eluents were premixed, thoroughly degassed with helium and filtered with membrane filters prior to their use. The injection volume ranged between 2 and 10 μl depending on column volume. The detection wavelength was 254 nm and all experiments were carried out at controlled room temperature (21 °C).

2.5. Analysis of dispersion data

Signal response obtained under nonretained conditions is usually characterized by asymmetric peak shapes whereas the asymmetry mainly depends on the tracer residence times in the column. It is, thus, necessary to deconvolute the detector signal into two functions: (i) a Gaussian function describing the signal variance caused by extra- and intracolumn band broadening, and (ii) a first order exponential decay function resulting in a time constant for first order dilution effects. The latter one accounts only for peak tailing due to incomplete axial equilibrium and increases as tracer residence times decrease. In order to distinguish between these complementary effects a convenient approach consists of using an exponentially modified Gaussian function (EMG) [49–51]:

$$f(t) = y_0 + \frac{h_0\sigma_t}{\tau}\sqrt{\frac{\pi}{2}}\exp\left[\frac{1}{2}\left(\frac{\sigma_t}{t}\right)^2 - \frac{t-t_0}{\tau}\right] \times \left\{1 - \mathrm{erf}\left[\frac{1}{\sqrt{2}}\left(\frac{\sigma_t}{t} - \frac{t-t_0}{\tau}\right)\right]\right\} \quad (1)$$

where t_0, σ_t^2 and h_0 represent mean residence time, variance and area of the Gaussian function and τ is the time constant of the first order decay function. As the extracolumn system geometry and, hence, extracolumn band broadening remained identical for each column during the whole experiment, and by taking into account only the Gaussian part of the deconvoluted elution profile, it allows to suppress the influence of an incomplete axial equilibration and offers the possibility of comparing axial dispersion in different column geometries. Chromatographic data were therefore exported from ChemStation software and imported into Origin 6.0 (Microcal, Northhampton, USA) in order to fit each signal response by an EMG. A transformation of the Einstein diffusion equation yields the apparent axial dispersion coefficient D_{ax} describing the sum of the intra- and extracolumn dispersion effects as derived from the detector output:

$$D_{ax} = \frac{\sigma_L^2}{2\Delta t} = \frac{u_{av}^2\sigma_t^2}{2t_{el,i}} \quad (2)$$

A time-scale-based signal response variance, however, has to be transferred into a length-scale-based variance by multiplication with the square of the average mobile phase velocity.

2.6. Analysis of adsorption data

Adsorption isotherms of caffeine on particulate

and monolithic RP18e material were determined via frontal analysis at room temperature. Eluent composition was the same as with the van Deemter analysis and the retention factor was kept at $k' = 5$ for all materials. Step gradients were run by the gradient pump at constant superficial velocity of 1 mm s^{-1} with pure mobile phase in the first and caffeine solution (20 mg/ml in the eluent) in the second channel. The accuracy of the step gradient was confirmed a priori with an acetone solution (0.5%, v/v), confirming a deviation below 1% for all steps. To avoid exceeding the detector's dynamic range the detection wavelength was 300 nm. The inflection point of each step was determined by fitting a Boltzmann function through the corresponding breakthrough curve. The calculation of adsorption isotherms was carried out as described in the literature [52].

3. Results and discussion

3.1. Hydraulic permeability

Unconsolidated porous media (either particulate or monolithic) usually exhibit a macroscopically coherent pore network system as evidenced by the average macropore diameters seen in the pore size distributions (Fig. 2), together with an inspection of scanning electron microscopy (SEM) pictures (Fig. 1) which reveal irregular, but geometrically congruent media. Even though these systems are macroscopically homogeneous (i.e. time and length scales on which transport processes occur are much smaller than the scales of variations in the velocity field experienced by the analyte) all porous media are characterized by a more or less broad distribution of diameter, characteristic lengths and shape (thus, morphology) of their respective interparticle (or interskeleton) macropore system, resulting in microscopically disordered structures. The general physical law governing flow resistance to a Newtonian fluid through such a fixed bed (particulate or monolithic) is Darcy's law (Eq. (3)), which presents a linear relationship between cross-sectional averaged superficial velocity and pressure gradient over the length of the bed [43]:

$$u_{sf} = -\frac{K}{\eta}\nabla p \tag{3}$$

This linear relationship is valid for the case of laminar flow and that both the Newtonian fluid and porous medium remain incompressible.

The hydraulic permeability data for (porous and nonporous) particulate and monolithic resins are shown in Fig. 4a. These data indeed confirm a linear increase of pressure drop (per metre) over the whole velocity range which reproduces nothing else than Darcy's law. For each material the flow regime remains in the laminar regime and both the bed and

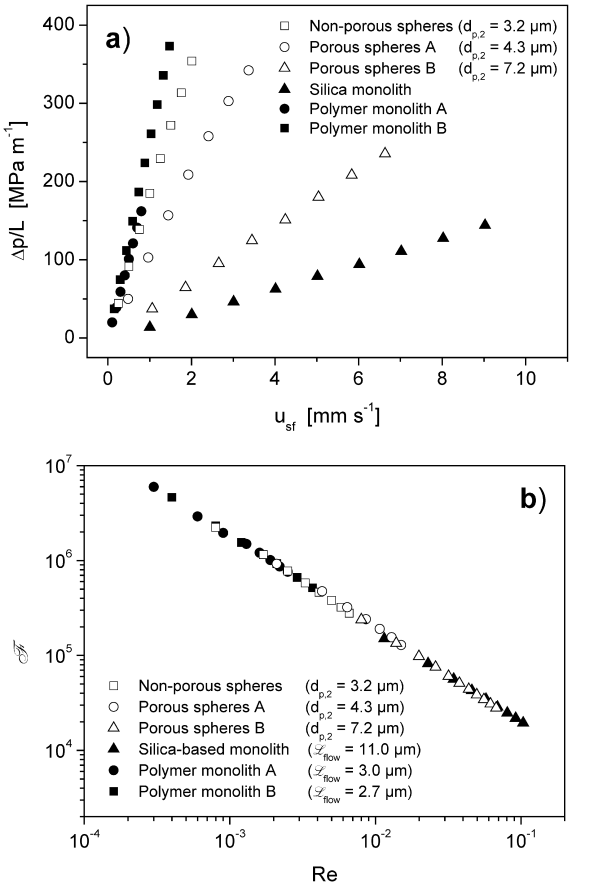

Fig. 4. Hydraulic permeability (using water as a liquid) of particulate and monolithic beds. (a) Flow resistance against superficial velocity, (b) dimensionless Darcy–Weißbach friction factor–Reynolds number relation (with $\bar{d}_{p,2}$ as $\mathscr{L}_{flow}$ for the particulate media, leading to $\mathscr{L}_{flow}$ for the monoliths via scaling of their data).

fluid can be regarded as being incompressible. Besides the fact that particulate media show different slopes according to their different particle dimensions this figure, in general, reveals quite strong differences in hydraulic permeability, especially between organic polymer and silica-based monoliths. The silica monolith offers the highest permeability of the systems investigated, while both polymer monoliths show a permeability less than that of a random-close packing of the smallest particles, i.e. the nonporous beads with an average diameter of 3.2 μm. Although these curves already indicate some trends, for a quantitative treatment of hydraulic permeability accounting for different interstitial porosities and particle diameters (as indicated by $\mathscr{L}_{\text{flow}}$ in Fig. 3) a transformation of the absolute data into a dimensionless form has to be performed and first properly applied to the particulate beds. Then, a direct comparison of the monolith's hydraulic permeability to those of particulate beds can be carried out by defining an appropriate characteristic length ($\mathscr{L}_{\text{flow}}$) for which both types of curves (monoliths, particulate beds) coincide.

Due to the fact that the specific permeability K can be determined exactly from Darcy's law but, vice versa, an exact prediction of the actual bed permeability from its characterizing macroscopic properties like porosity or average pore diameter fails, simplified geometrical models of the pore network (especially for particulate fixed beds) were developed to allow an estimation of the bed's permeability by knowing macroscopic properties like the interstitial porosity, mean particle shape or diameter [44–46].

For example, the Kozeny–Carman equation [53] is based on the assumption that an irregular distribution of pore dimensions in a fixed bed of particles can be replaced by a bundle of twisted, nonintersecting channels with a similar diameter in which flow resistance is governed by the Hagen–Poiseuille law for laminar flow in open tubes. If the permeability data shall be normalized through this approach also the limitations of this model have to be considered: the equation is based on empirical data that were acquired for random-close packings of nearly spherical particles, having narrow particle size distribution and an interstitial porosity of about 0.4 [53]. An extension of the porosity function obtained for this model to porous media with an interstitial porosity much higher than that of a random-close sphere packing is physically not consistent and will therefore lack accuracy. Despite such restrictions the Kozeny–Carman equation gives reasonable results when permeability data based on similar column and particle dimensions are considered [47]. To avoid limitations and allow for a comparison of chromatographic media with very different porosities we here adopt the approach of the dimension analysis. This phenomenological approach was used by Rumpf and Gupte [54,55] in their study of liquid flow through porous media covering a wide range of porosities (for $10^{-2} \leq Re \leq 10^{2}$, using sphere packings prepared by a special procedure, with interparticle porosities between 0.35 and 0.68). In dimension analysis all the experimentally available system parameters are first defined and then calculated against each other, leading to a dimensionless number which specifically characterizes the system under investigation.

In the case of laminar flow of a Newtonian fluid through a fixed bed (fluid and bed are considered incompressible and, therefore, Darcy's law is valid) the general approach of dimension analysis for hydraulic permeability can be represented as [55]:

$$\frac{\Delta p}{\rho u_{\text{sf}}^2} = f\left(Re = \frac{u_{\text{sf}}\bar{x}}{\nu}, \frac{L}{\bar{x}}, \varepsilon_{\text{inter}}, q_i, \psi_i, \text{packing structure}\right) \quad (4)$$

System parameters affecting flow resistance are: (i) total pressure drop Δp over the fixed bed, (ii) cross-sectionally averaged superficial velocity u_{sf}, and (iii) volumetric density of the liquid ρ. Their ratio (see left-hand side of Eq. (4)) is a function of several also dimensionless variables characterizing liquid flow, packing material and structure: (i) Reynolds number, (ii) interstitial porosity $\varepsilon_{\text{inter}}$, (iii) particle shape and size distribution factors (ψ_i and q_i) and (iv) the ratio of bed length L divided by a mean characteristic length $\bar{x}$ of the porous medium orthogonal to the flow direction which governs the flow resistance, defined as $\mathscr{L}_{\text{flow}}$ for both the particulate and monolithic media. In a random-close packing for which L strongly exceeds $\mathscr{L}_{\text{flow}}$ all factors affecting the axial flow resistance can be considered as constant over the bed length, leading to a linear

relationship between $\Delta p/(\eta u_{sf}^2)$ and $L_{bed}/\mathscr{L}_{flow}$, summarized in the Darcy–Weißbach friction factor $\mathscr{F}$:

$$\mathscr{F} = \frac{\Delta p}{\rho u_{sf}^2}\frac{\mathscr{L}_{flow}}{L_{bed}} = f\left(Re = \frac{u_{sf}\mathscr{L}_{flow}}{\nu}, \varepsilon_{inter}, q_i, \psi_i\right) \quad (5)$$

The (dimensionless) Darcy–Weißbach friction factor itself is a function of several dimensionless parameters but if spherical particles with a narrow particle size distribution are used, deviations in the interstitial porosity, particle shape and size distributions have a negligible influence, reducing $\mathscr{F}$ to a function of only one dimensionless variable, the Reynolds number. Taking $\mathscr{L}_{flow}$ as the mean surface-averaged particle diameter, the friction factor–Reynolds number relation for the different sphere packings leads to a coincidation of these data onto a linear master curve (open symbols in Fig. 4b), justifying the assumption that the phenomenological approach of dimension analysis is well suited for comparing different sphere packings, porous and nonporous, and that also the resulting packing properties in view of ε_{inter}, q_i, and ψ_i are sufficiently similar. (Because the viscous drag on a spherical particle in laminar flow is proportional to the surface area orthogonal to the flow direction [10], it is physically meaningful to use the mean surface-averaged particle diameter $d_{p,2}$ for characterizing $\mathscr{L}_{flow}$. Also other authors dealing with the flow resistance in porous media have used $d_{p,2}$ [46,55].)

The close correlation of hydraulic permeability data for porous and nonporous beads suggests an extension of this phenomenological approach to the monolithic resins in order to relate their specific permeability data to those of particulate beds simply by scaling them with an appropriate $\mathscr{L}_{flow}$ to the particles' master curve (closed symbols for the monoliths, Fig. 4b). The data for both silica-based and polymer monoliths fit well into the master curve, suggesting the usefulness of this approach. The equivalent sphere dimensions for permeability ($\mathscr{L}_{flow}$) are 3.0 μm and 2.7 μm for the polymer monoliths A and B, respectively, whereas the permeability of the silica monolith equals that for a fixed bed of 11.0 μm spheres ($d_{p,2}$). Differences in flow resistances between the monolithic resins are more difficult to explain by only their mean individual bed properties. For example, based on macropore diameters (and by considering the Hagen–Poiseuille law) the expected permeability ratio concerning the silica and polymer monoliths should be about 4, but it actually ranges between 12 and 16. Certainly the porosities also need to be considered here, but because the monoliths span a quite substantial range of porosities, the resulting difficulty lies in the estimation of an accurate porosity function which is able to cover the total range. Already an extrapolation based on the Kozeny–Carman equation for sphere packings with higher interstitial porosity than the typical 0.4 becomes inaccurate. For example, as shown by Rumpf and Gupte the porosity function $(1-\varepsilon_{inter})^2/\varepsilon_{inter}^3$ after Blake, Kozeny and Carman should be better replaced by $\varepsilon^{-5.5}$ or by the still more meaningful function $4(1-\varepsilon_{inter})\varepsilon_{inter}^{-4.55}$ [55].

Hence, there seems to exist no clear relationship between bed structure properties like porosity or macropore diameter and permeability according to Darcy's law (cf. $\mathscr{L}_{flow}$ and Table 1). It points towards the usefulness of a pragmatic approach, to relate hydrodynamic properties of monoliths to those of the well-defined and understood system comprised by a fixed bed of spheres via the phenomenological approach of dimension analysis, taking into account only directly measurable macroscopic system properties.

Absolute permeability data for various organic polymer-based monoliths adapted from the literature were subsequently scaled to obtain $\mathscr{L}_{flow}$ with the help of particulate reference materials and with water as the liquid. The resulting equivalent sphere dimensions are listed in Table 2. Data for the commercially available polymer monoliths A and B adapted from different authors reveal that the permeabilities of these monoliths result in an $\mathscr{L}_{flow}$ of similar magnitude as in this study. Polymer-based monolithic resins offer an individual permeability characteristic depending on preparation conditions. Therefore, no general relationship between the nature of these monolithic stationary phases (organic polymer or inorganic silica skeleton) and permeability can be drawn.

A phenomenological approach relying on the Darcy–Weißbach friction factor–Reynolds number

Table 2
Relative permeability of selected monolithic materials

Author	Svec et al.	Wang et al.	Liao et al.	Mayr et al.	Premstaller et al.	Luo et al.	Hahn et al.	Ghose et al.
Year	1992 [15]	1994 [16]	1996 [56]	2001 [57]	2000 [58]	2001 [59]	2001 [60]	2001 [61]
Type of monolith	HPLC-format polymer monolith, laboratory-made	HPLC-format polymer monolith, laboratory-made	Capillary polymer monolith, laboratory-made	HPLC-format polymer monolith, laboratory-made	Capillary polymer monolith, laboratory-made	HPLC-format polymer monolith, laboratory-made	HPLC-format polymer monolith, CIM Disk	HPLC-format polymer monolith, UNO S
Purpose of use	Ion-exchange liquid chromatography of proteins	RP liquid chromatography of peptides and alkylbenzenes	Electro-chromatography of polycyclic aromatic hydrocarbons	Liquid chromatography of proteins and oligonucleotides	Ion pair RP chromatography of oligonucleotides	Immobilized metal affinity chromatography of proteins	Analysis of hydrodynamics	Analysis of hydrodynamics
$\mathscr{L}_{\mathrm{flow}}$ (μm)	5.5	9.5	16.0	16.0	2.5	11.5	2.5	3.5

relation, which is not based on any confining model and which takes into account only directly measureable system parameters, is shown to be a sufficient, yet extremely practical tool for the dimensionless scaling of permeability data for porous media with a quite different porosity and structure. By introducing the radial length scale $\mathscr{L}_{\mathrm{flow}}$ (an equivalent sphere diameter for hydraulic permeability), it is possible to attribute to each monolithic bed a single value which describes its macroscopic permeability in terms of the average particle diameter of spheres in the equivalent sphere packing and, thus, allows a convenient and straightforward comparison of monolithic and particulate chromatographic beds, at least under this point of view.

3.2. Hydrodynamic dispersion

For a quantitative comparison of the axial dispersion coefficients of the solute a method has to be devised which also allows to evaluate the apparently diverging data for the various media in a dimensionless form. Prerequisite is a constant and sufficiently small extracolumn contribution to the band broadening. Then, a possible approach consists of applying the Van Deemter model for band dispersion in chromatographic media [62] which uses the theoretical plate height (H), an already reduced parameter, for indicating the effectiveness of a column via the first derivative of the axial variances of the detector response signals with respect to the column length (i.e. $H = \mathrm{d}\sigma_{\mathrm{L}}^2/\mathrm{d}L$). The introduction of three parameters for mechanical (eddy) dispersion, axial molecular diffusion and nonmechanical dispersion (stagnant mobile phase mass transfer) results in the well-known Van Deemter equation in which all processes are considered to occur independently and, therefore, their offered resistances add in series. Then, the dispersion data for silica-based monoliths with a bimodal pore size distribution can be scaled on the basis of a lumped mass transfer kinetics (C-term parameter) to those observed for fixed beds of porous spheres (also with a bimodal pore size distribution cf. Fig. 2) by introduction of an equivalent sphere dimension concerning axial dispersion [47]. For this purpose, the mass transfer in the stagnant part of the mobile phase, here the intraskeleton or intraparticle pore space, has to remain diffusion-limited (as a function of Pe) in order to use the Van Deemter equation. Reduced plate height plots originating from the dispersion data for particulate and monolithic beds then may coincide by appropriate dimensionless scaling.

To verify this simple approach with uncharged analyte molecules on reversed-phase materials, Van Deemter curves for monolithic columns with different surface modification (RP4e, RP8e and RP18e), as well as for a 3.0 μm particulate RP18e ‘‘reference’’ material are shown in Fig. 5. They were obtained with caffeine under strong retention conditions ($k' = 5$). Regression data for both the A-term and C-term parameters are (for all the reversed-phase monolithic media) very similar to those for the random-close packing of these 3.0 μm spheres (cf. Table 3). Thus, the monoliths equivalent particle diameter for axial dispersion representing that in a bed of completely porous spheres of 3 μm (this dimension is obtained here without the need for concrete calculation of the C-term parameter, but just—accidentally—by optical inspection) is consistent with our previous findings [47]. One advantage of the Van Deemter analysis is a convenient direct derivation based on readily obtainable plate height curves of equivalent sphere dimensions for axial dispersion under conditions of retained elution. These conditions guarantee relatively long tracer residence times in the column, resulting in accurate experimental data concerning the C-term

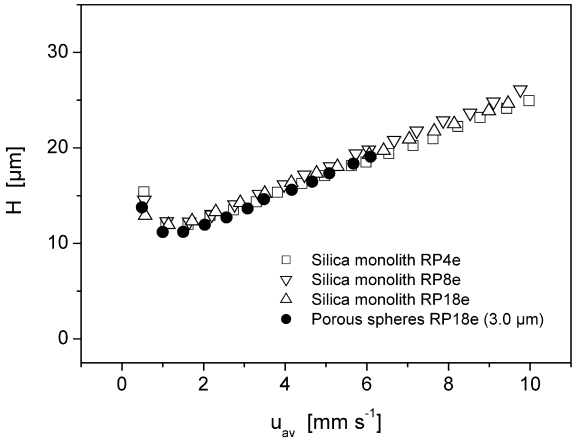

Fig. 5. Van Deemter curves for caffeine on silica-based monolithic and particulate stationary phases obtained under conditions of strong retention ($k' = 5$).

Table 3
Van Deemter parameters for caffeine elution

Stationary phase	A (μm)	B_{calc} (10^{-9} m^2/s)[a]	C (10^{-3} s)
Silica monolith RP4e	10.1±0.5	0.7	1.4±0.1
Silica monolith RP8e	10.0±0.4	0.7	1.6±0.1
Silica monolith RP18e	9.7±0.2	0.7	1.6±0.1
Fixed bed of spheres RP18e	9.3±0.6	0.7	1.5±0.2

[a] $B_{calc} = 2k_b D_m$ with k_b being the obstruction factor (0.7), and $D_m = 0.5\times10^{-9}$ m^2/s [62].

(significant slope in the plate height curves) which then clearly dominates the overall dispersion. But, at the same time, the use of retained conditions is also one of the major drawbacks of this approach. Comparisons of dispersion behaviour will then be complicated by the surface-specific adsorption kinetics, in addition to the differences in diffusion path lengths in the particulate and monolithic materials. Thus, the main focus of this work (the hydrodynamic dispersion) will be, at least partly, obscured by thermodynamic effects. To circumvent these difficulties elution under nonretained conditions is favored because dominating mass transfer resistances in the mobile phase then arise from diffusive processes that itself originates in stagnant zones characterized by a different spatial dimension (and pore space morphology), depending on the material under consideration. But, as a consequence, the C-term parameter is then reduced to a magnitude which represents the actual experimental error in its determination and this, in turn, prohibits a meaningful data evaluation.

Therefore, the plate height H is first replaced by the dispersivity $\mathscr{D}$, the dimensionless ratio of the effective axial dispersion coefficient to the analytes molecular diffusivity. By applying dimension analysis to axial dispersion in fixed beds of porous spheres we can formulate Eq. (6), describing $\mathscr{D}$ as a function of several (also dimensionless) factors [48]:

$$\mathscr{D} = \frac{D_{ax}}{D_m} = f\left(Pe = \frac{u_{av}\mathscr{L}_{disp}}{D_m}, \varepsilon_{inter}, q_i, \psi_i, \varepsilon_{intra}, \frac{D_{stag}}{D_m}\right) \quad (6)$$

The same parameters as for the permeability data are used to characterize interstitial porosity, particle shape and size distribution, and they can be neglected for a random close packing of spheres with relatively narrow particle size distribution and reasonable sphericity. $\mathscr{D}$ depends on the Peclet number, on intraparticle porosity and reduced pore diffusivity (D_{stag}/D_m), where D_{stag} is the effective diffusion coefficient of analyte molecules in the stagnant zone. However, in order to scale the dispersion data for porous and nonporous spheres via dimension analysis in a similar way as for the permeability data, we have to introduce a common (appropriate) length scale $\mathscr{L}_{disp}$ for the consistent determination of the dispersive flow regime (cf. Eq. (6)).

For studying the axial dispersivity $\mathscr{D}$ of a neutral, nonreacting solute in incompressible liquid flow through a random sphere packing as a function of Pe we have to take into account the bed's tortuosity (τ_{bed}), a mechanical dispersion contribution (coefficient Θ_m) and two nonmechanical mechanisms, namely boundary-layer mass transfer (Θ_b) and the liquid hold-up in the intraparticle stagnant zone (Θ_h) [63]:

$$\mathscr{D} = \frac{D_{ax}}{D_m} = \tau_{bed} + \Theta_m Pe + \Theta_b Pe \ln(Pe) + \Theta_h Pe^2 \quad (7)$$

Apparently, the liquid hold-up contribution is not present with nonporous particles (unless some of the particles crush and lead to an appreciable amount of dead-end blockage, or the ''nonporous'' particles have micropores to a finite extent). The relevant flow regime for mechanical dispersion and boundary layer mass transfer can be characterized by $\mathscr{L}_{flow}$ because both contributions are physically related to the (velocity and shear stress at/close to the) particles external surface. By contrast, the liquid hold-up in beds of porous spheres is inherently coupled to $\mathscr{L}_{stag}$ (cf. Fig. 3), the effective intraparticle diffusion pathlength that we determine, in this study, for

completely porous spherical particles from their mean surface-averaged particle diameter ($\bar{d}_{p,2}$).

In beds of nonporous spheres, i.e. in the absence of liquid hold-up, $\mathscr{L}_{disp}$ is determined uniquely by $\mathscr{L}_{flow}$, but for the porous particles both $\mathscr{L}_{flow}$ and $\mathscr{L}_{stag}$ are important. Apparently, they are not identical (Fig. 3). The intraparticle liquid hold-up contribution begins to dominate axial dispersion when completely porous spheres are used and Peclet numbers *Pe* sufficiently exceeding unity are encountered ($Pe > 20$; it is, thus, most relevant in liquid chromatography practice). This has been re-evaluated and demonstrated recently by the complementary pulsed field gradient NMR measurements, combined with a numerical simulation (using high-resolution flow fields) of axial dispersion coefficients in packings of porous and nonporous spherical particles (Fig. 6a) [64], an aspect to which we will return to below.

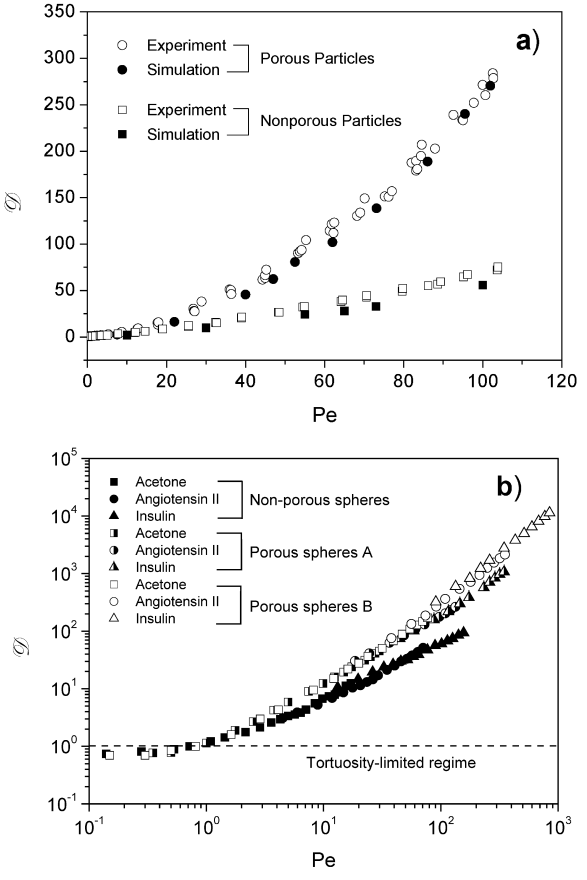

Fig. 6. Dimensionless dispersivity versus the Peclet number for random packings of totally porous and nonporous spheres. (a) Data obtained with PFG-NMR measurements and numerical simulations, reprinted with permission from Kandhai et al. [64]. Regression analysis results in the following values for τ_{bed}, Θ_m, Θ_b, and Θ_h: 0.74, 0.144, 0.101 and 0.020 in the case of the porous particles, and 0.51, 0.153, 0.080 and 0.0016 for the nonporous spheres. (b) Data obtained by tracer elution experiments under unretained conditions. For all curves (porous or nonporous particles) *Pe* has been calculated, as is usually done, on the basis of the mean particle diameter.

Axial dispersion in random-close packings of totally porous and completely nonporous spheres represents two limiting cases for which the flow regime can be conveniently characterized by a single length scale ($\mathscr{L}_{disp}$) which is $\mathscr{L}_{stag}$ in the former and $\mathscr{L}_{flow}$ in the latter situation. The actual flow regime for pellicular particles (cf. Fig. 3), however, needs two different length scales and the dimensionless dispersivity is not expressed easily in a reduced form. Because liquid hold-up in these particles is strongly reduced (this is one of the main purposes of the pellicular particles), it may not be the dominating contribution to band dispersion any longer, yet not be negligible, and $\mathscr{L}_{disp}$ cannot be replaced simply by $\mathscr{L}_{stag}$ without introducing an ambiguity.

Before we continue with a demonstration of the importance of liquid hold-up in stagnant zones for a determination of an equivalent dispersion length for monoliths compared with that in particulate beds, it should be pointed out that Eq. (7) apparently contains a coupling (via the boundary-layer contribution) between mechanical dispersion and mass transfer resistances arising in the mobile phase. This is in contrast to the Van Deemter model (*A*-term independent of velocity) and it is still incomplete compared to the Giddings coupling theory [8]. Giddings has addressed the important role played by lateral diffusion (or, more correctly, by lateral dispersion, although it is only a very weak function of *Pe*) in the relaxation of radial concentration gradients. For this purpose, he has identified several velocity inequalities of the flow pattern in a packed bed, covering length scales from the radius of an individual interparticle pore (transchannel contribution), via short and long range interchannel effects (including a few particle diameters), up to the whole diameter of the column (transcolumn contribution) [65]. For the sake of completeness, Eq. (7) expresses

coupling only between the pore-scale velocity inequality arising due to the no-slip condition at the solid–liquid interface and diffusion normal to that surface. This pore-level Taylor dispersion translates to the Giddings transchannel effect. Velocity inequalities on a higher length-scale (like short and long range interchannel, or even transcolumn effects) are not considered [63]. Thus, ''coupling'' between mechanical and nonmechanical effects in Eq. (7) represents a situation between the Van Deemter model and the comprehensive Giddings equation [8]. Nevertheless, the importance of intraparticle liquid hold-up, irrespective of the foregoing discussion, stems from the fact that this contribution (proportional to $\Theta_h Pe^2$, cf. Eq. (7))—as there is no flow inside the particles and, thus, no coupling with mobile phase velocities—starts to dominate overall dispersion at higher values of *Pe*. But how high must *Pe* get to clearly distinguish between mechanical and nonmechanical effects? The answer is provided by Fig. 6a.

By having used well-defined computer-generated, as well as physical sphere packings of porous and nonporous particles, lattice-Boltzmann flow field simulations and pulsed field gradient NMR measurements have revealed (Fig. 6a), in excellent agreement, that for both types of particles (porous and nonporous) the parameters for mechanical dispersion and boundary-layer mass transfer are indeed very similar (most probably because surface chemistries, particle shape and size, as well as their distribution parameters were comparable), but that the coefficient for liquid hold-up shows an increase by more than a decade with the porous particles [64]. It should also be mentioned that both columns (porous vs. nonporous particles) were packed and consolidated by the same procedure. As clearly demonstrated in Fig. 6a the liquid hold-up contribution starts to dominate dispersion in the bed of porous spheres at Peclet numbers exceeding about 20. Thus, liquid hold-up as a particular dispersion mechanism is also suited to study and compare the band broadening in monolithic and particulate beds, as long as this contribution is sufficiently present in a material and dispersion data are acquired over a sufficiently wide range of *Pe*.

Compared to these results based on the direct measurement and simulation of axial dispersive processes in packed beds, the classical chromatographic tracer dispersion data derived from an external detector response are strongly affected by the respective extracolumn volumes and, therefore, are usually more scattered (Fig. 6b). Dispersion data for porous particles A and B (cf. Table 1) in Fig. 6b have a different dependence of $\mathcal{D}$ on *Pe*, caused mainly by differences in the intraparticle porosity and different reduced pore diffusivities D_{stag}/D_m (Table 4), as both quantities contribute to the coefficient Θ_h characterizing the liquid hold-up. Consequently, these parameters (ε_{intra} and D_{stag}/D_m) also directly influence the slope of dispersivity curves in a regime where the hold-up contribution dominates the overall dispersion [48].

The direct comparison of axial dispersion in monolithic and particulate media having a bimodal pore size distribution (one set of pores for convection-dominated transport, the other set of pores for achieving a large surface area, but with diffusion-limited mass transfer) can be accomplished, in analogy to the permeability data, by defining an $\mathcal{L}_{stag}$ for the monolithic structures so that their dispersion data collapse onto the dispersivity curve for the particulate media. This dimensionless scaling strategy will work perfectly when both axial dispersion curves (i.e. for the monolithic and particulate beds) are characterized by a similar slope, meaning

Table 4
Physical properties of the tracer molecules used in dispersion analysis

Tracer	Molecular mass (g/mol)	R_G (nm)	D_m (10^{-10} m^2/s)	D_{stag}/D_m			Ref.
				Porous spheres A	Porous spheres B	Silica monolith	
Acetone	58.1	n.a.	12.8	0.35	0.50	0.64	[66]
Angiotensin II	1046	<0.2	3.1	0.20	0.37	0.36	[67]
Insulin	5807	0.54	1.4	0.14	0.29	0.25	[68,69]
BSA	67 000	3.06	0.6	0.05	Size exclusion	Size exclusion	[70]

that the reduced effective pore diffusivities (cf. Table 4 and the list of symbols) become similar. Otherwise, the dispersivity plots will not coincide exactly, a behaviour that is well known from the reduced plate height curves for different particulate media in liquid chromatography.

The elution under nonretained conditions allows to derive the effective total porosity experienced by each analyte from its residence time distribution (Table 5). Acetone, angiotensin II and insulin are able to enter the intraparticle or intraskeleton pore space of all silica-based chromatographic materials. Further, liquid hold-up dominates dispersion at $Pe \gg 1$ in these hierarchically-structured porous materials (with intraparticle or intraskeleton mesopores and interparticle or interskeleton macropores). For the porous spheres B and the silica-based monolith the dispersion data for all analytes demonstrate a unique behaviour when defining an $\mathcal{L}_{stag}$ for the monolith of 1.0 μm (Fig. 7a). This actually means that dispersion in this monolithic structure corresponds to (is equivalent to) that in a random close packing of porous spheres with an average particle diameter of 2.0 μm having similar stagnant zone pore space morphology as the porous spheres B (which were used as a ''reference'' in this analysis). In contrast to the above-mentioned analytes, effective porosity data for BSA elution (Table 5) indicate that this molecule is size-excluded from the mesoporous intraparticle pore space of the porous spheres B and also from the mesoporous skeleton of the silica monolith (see also Table 1). Because BSA does not experience a substantial liquid hold-up (if any at all—boundary layer mass transfer resistance is still present and it is certainly diffusion-limited close to the surface, normal to it, but its characteristic length-scale is small and it does not constitute a liquid hold-up mechanism) and undergoes convec-

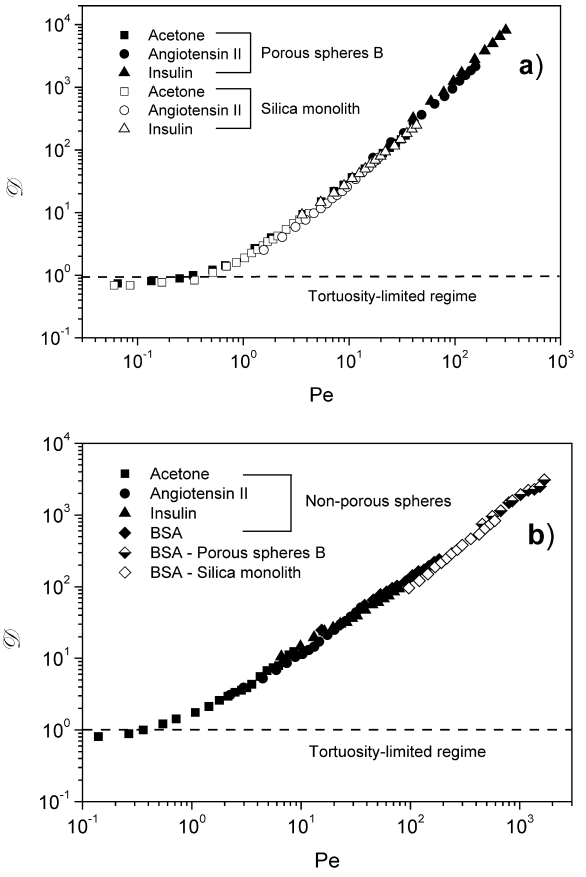

Fig. 7. Dimensionless scaling of tracer dispersion data for the silica-based monolith. (a) Axial dispersivity in the monolithic structure and in the random packing of porous particles B, with the analyte experiencing liquid hold-up in the stagnant part of the mobile phase (intraparticle or intraskeleton pore space). The data are plotted and scaled versus *Pe* calculated based on the thickness of the porous layer of completely porous particles which is $\bar{d}_{p,2}/2$ (cf. Fig. 3). This procedure leads to an $\mathcal{L}_{stag}$ for the monolith of 1.0 μm. Reprinted with permission from Tallarek et al. [48]. (b) $\mathcal{D}$ vs. *Pe* for the nonporous spheres, together with the BSA elution data for porous spheres B and the monolith (size exclusion). In all cases, *Pe* is now calculated based on $\mathcal{L}_{flow}$.

Table 5
Effective tracer porosities in the different porous media

Tracer	Sphere packings			Monoliths		
	Nonporous	Porous spheres A	Porous spheres B	Silica-based	Organic polymer A	Organic polymer B
Acetone	0.36	0.65	0.75	0.92	0.70	0.47
Angiotensin II	0.36	0.55	0.68	0.84	0.60	0.35
Insulin	0.36	0.51	0.63	0.80	0.58	0.34
BSA	0.36	0.37	0.36	0.70	0.55	0.32

tion-dominated dispersion in the interparticle or interskeleton pore space, these dispersion data resemble more those for beds of nonporous spheres. Then, the best measure for $\mathscr{L}_{\mathrm{disp}}$ in this limiting case appears to be $\mathscr{L}_{\mathrm{flow}}$ like $d_{\mathrm{p},2}$ for the nonporous particles, as pointed out earlier. By representing the BSA dispersion data with an $\mathscr{L}_{\mathrm{flow}}$ of 11.0 μm for the silica monolith (obtained from the permeability analysis) and 7.2 μm for the porous spheres B and by comparing these data to those for the packing of nonporous spheres, we arrive at a unique scaling and finally obtain an equivalence for the axial dispersion behaviour in the interstitial (interparticle or interskeleton) pore space of these media (Fig. 7b).

The axial dispersion data for both polymer monoliths could not be scaled in a meaningful way to the behaviour observed in the reference beds of porous or nonporous particles. While the pore size measurement by mercury intrusion and a surface area determination by nitrogen adsorption could not prove any significant amount of micro- and/or mesopores, the effective porosity data in Table 5 indicate that these two monoliths are not completely nonporous concerning liquid hold-up meaning that their pore size distribution (Fig. 2) remains not necessarily monomodal for all of the analytes. Moreover, the data for polymer monolith B cannot be further differentiated because of the relatively high extra-column volume engendered by the disk housing system (cf. Table 1).

3.3. Adsorption capacity

In preparative chromatography the sample amount loaded on a column is increased to a stage in which the surface concentrations of adsorbed analyte molecules cannot be treated independent from the already adsorbed molecules any longer and the adsorption isotherm begins to show a nonlinear behavior [52,71,72]. In view of high-throughput processes, stationary phase materials have to be designed for nonlinear chromatography which offer large specific surface areas [73]. This aspect clearly favours completely porous support structures over nonporous ones (Table 1). Differences in the maximum loading capacity for different stationary phases can be derived from the determination of the adsorption isotherms under identical retention conditions, preferably for molecules obeying a Langmuir isotherm type [73] because the monolayer saturation capacity, in contrast to the nitrogen adsorption data, inherently contains the influence of the respective pore space morphology, e.g. it accounts for differences in accessible pore space for larger analytes.

All adsorption isotherms in this study were determined by frontal analysis [74–78] under strong retention conditions ($k' = 5$) for RP18e porous spheres and the silica monoliths with RP4e, RP8e and RP18e surface modification. Caffeine was chosen as analyte because it adsorbs reversibly on reversed-phase materials and shows Langmuir behaviour (as has been determined a priori). Further, its high solubility in water (of more than 20 g l^{-1}) allows to realize sufficiently high surface concentrations so that the monolayer saturation capacity can be approached. Adsorption studies were not carried out for polymer monoliths because both are fabricated from different monomers and, therefore, they show different SCX surface characteristics. Moreover, a suitable (polymer-based) particulate reference material was not available. In addition, an extensive capacity study for proteins on polymer monolith B has already been published [33].

For complementary information about the specific adsorption behaviour of caffeine, its adsorption isotherms were plotted with respect to the following parameters (Fig. 8): volumetric solid-phase concentration (mass of caffeine per stationary phase volume), surface concentration (mass of caffeine per BET surface area of the solid-phase), and the relative column volume-weighted concentration (mass of caffeine per column volume). Differences in phase ratio between the two columns (particulate and monolithic bed) indicate that the volume-weighted adsorption isotherm, although useful for modelling chromatograms with a single stationary phase [71], is not suited for describing variations in adsorption capacity for different materials because adsorption occurs on the surface of the solid, but not within its volume. Therefore, the adsorption is better represented by the surface-weighted isotherm, indicating that the monolith's loading capacity (per squared metre of the BET surface area) is increased compared to sphere packings with a similar surface modification. But also this illustration allows only limited conclusions about adsorption behaviour on

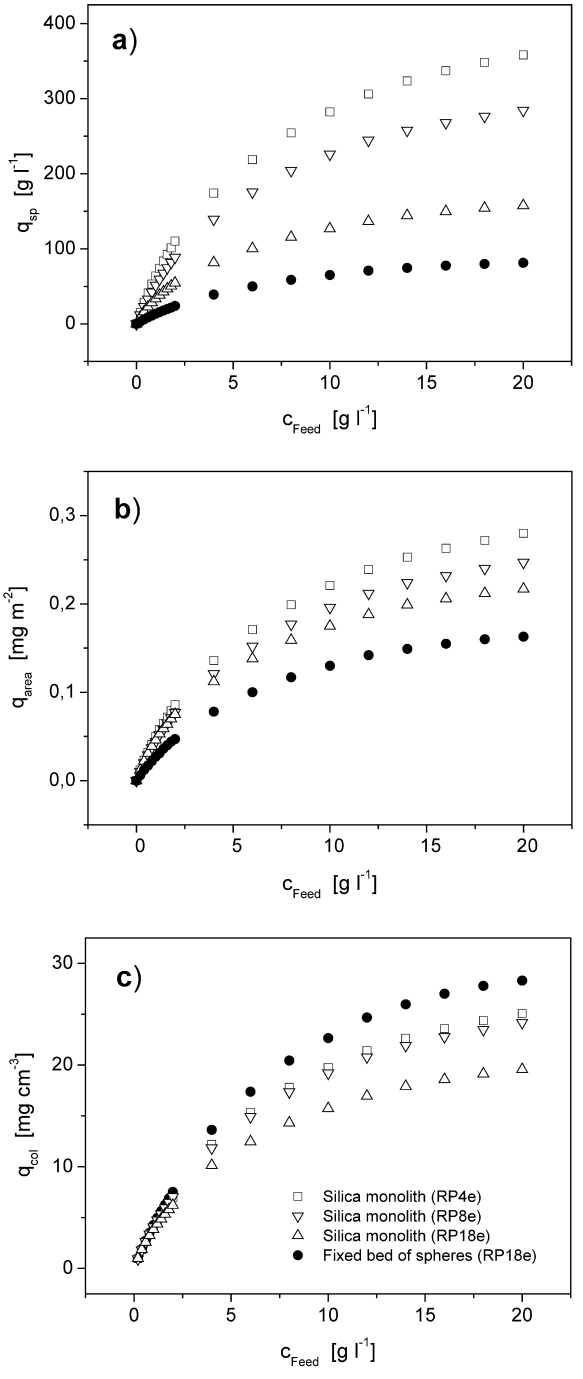

Fig. 8. Adsorption of caffeine on monolithic and particulate stationary phase materials under conditions of strong retention. Reference parameter: (a) the solid-phase concentration (q_{sp}), (b) solid-phase surface concentration (q_{area}), and (c) the column volume-weighted concentration (q_{col}).

different porous media, because the area determination was carried out by using nitrogen, a molecule assumed to enter the whole meso- and micropore space. However, the BET analysis does not describe the effective surface area for caffeine. Possible explanation for differences in surface loading capacities may be found in a reduced accessibility of parts of the pore network, (i) in reversed-phase modifications with longer chain lengths (RP18e) compared to materials with a shorter carbon chain (RP4e and RP8e) and (ii) in the silica spheres compared to monoliths due to the higher solid-phase content of the particles (cf. phase ratio in Table 1).

Quantitative information about adsorption capacity in different chromatographic beds is obtained by illustrating the adsorption isotherm with respect to the column volume-weighted concentration (Fig. 8c), because this representation includes the materials-specific adsorption and solid-phase content in the actual column. Adsorption data were fitted to the Langmuir isotherm and resulted in a maximum column volume-weighted loadability for the porous spheres of 40.4 mg/ml and one of 25.7, 33.1 and 34.9 mg/ml for the silica monoliths with RP18e, RP8e and RP4e surface modification, respectively. In all cases, regression coefficients were better than 0.999. Reduction of chain length from RP18e to RP8e and RP4e leads to a significant increase in the maximum adsorption capacity for the monolithic columns. A possible explanation may be found by a better accessibility of the mesopore space (combined with a larger effective surface area) when shorter chain lengths are used. In general, however, the silica-based monoliths offer a lower adsorption capacity than particulate beds, e.g. the monolayer saturation capacity for caffeine on the RP18e silica monolith is about 64% of that for the corresponding RP18e modified fixed bed of porous spheres. This difference is mainly caused by the actual amount of solid-phase in each column. In the particulate chromatographic beds the total mass of solid is about three times higher than for the highly porous silica monolith. But the significantly higher intraskeleton porosity, possibly also providing better accessible intraskeleton pore space, compensates partly the solid-phase ratio of these materials of only 0.34: the resulting surface ratio is 0.58 and the actual ratio of maximum loading capacities amounts to 0.64. Thus,

compared to conventional particulate stationary phase materials the silica-based monoliths with bimodal pore size distribution provide a still comparable and only slightly decreased dynamic adsorption capacity.

4. Conclusions

The phenomenological approach of dimension analysis, suitable for scaling the hydrodynamics in different fixed beds of (porous and nonporous) spheres via their mean particle diameter, also allows to relate hydraulic permeability and axial dispersion data for monolithic chromatographic supports to the behaviour of well characterized random-close packings of spheres. It is achieved by the introduction of equivalent sphere dimensions for the monolithic structures. Although the continuous solid-phase of monoliths leads to a different bed morphology, this approach provides an excellent competitive analysis concerning the hydraulic permeability of all monoliths (organic polymer, silica-based) and the axial dispersion behaviour of, at least, the porous silica monoliths. The hydrodynamics in these monoliths can now be characterized in terms of particle dimensions via single values of $\mathscr{L}_{\mathrm{flow}}$ and $\mathscr{L}_{\mathrm{disp}}$.

In general, the hydrodynamic properties of a porous medium can be described by the ratio of the aforementioned dimensions for axial dispersion and hydraulic flow resistance:

$$\mathscr{R}_{\mathrm{HP}} = \frac{\mathscr{L}_{\mathrm{disp}}}{\mathscr{L}_{\mathrm{flow}}} \tag{8}$$

It characterizes the hydrodynamic performance of stationary phases [48]. For completely porous spheres this ratio is 0.5 (Fig. 3), meaning that the mean sphere diameter, respectively the mean radius, can determine the flow regime for permeability and dispersion.

The hydrodynamic properties of the silica-based monoliths with a bimodal pore size distribution correspond to those of a bed of totally porous spheres with a radius of $\mathscr{L}_{\mathrm{stag}} = 1.0$ μm concerning dispersion originating in the monoliths mesopore space (under nonretained elution condition and with liquid hold-up in the mesopore space as the dominating contribution to the axial dispersion), as well as to a packing with equivalent sphere diameter for hydraulic permeability and dispersion in the macroporous interskeleton pore space of $\mathscr{L}_{\mathrm{flow}} = 11.0$ μm. The hydrodynamic performance ratio for analytes experiencing liquid hold-up thus is reduced to $\mathscr{R}_{\mathrm{HP}} = 0.09$. To realize this ratio in sphere geometry, pellicular particles have to be applied with a total diameter of 11 μm (as $\mathscr{L}_{\mathrm{flow}}$), and with a thickness of the porous layer (in the first approximation) of $\mathscr{L}_{\mathrm{stag}}$. However, a geometrical analysis of this diffusive layer suggests that its thickness can be treated as small in comparison with the total radius of the resulting solid core–porous shell sphere. This allows to apply the one-dimensional diffusion equation (Fick's second law) for infinite plane sheets [79,80] (i.e. for slab geometry) in the case of the pellicular particle. The corresponding thickness of the porous layer leading to a similar dispersion as the (completely porous) sphere with a radius $\mathscr{L}_{\mathrm{stag}}$ is derived by solving the diffusion equation in slab and sphere geometries for transient diffusion and assuming equivalent mean residence times of the analyte molecules in both media [81,82]. Rodrigues et al. [83,84] have solved this problem and have obtained a value of $1/\sqrt{5}$ for the ratio of the slabs half thickness to the sphere radius, assuming purely diffusive mass transport. Pellicular particles having an overall $d_{\mathrm{p}} = 11$ μm to account for permeability, with similar hydrodynamic performance ratio as the silica-based monoliths (i.e. $\mathscr{R} = 0.09$), then have a porous layer that is only 0.45 μm thick. For such a pellicular particle, the resulting nonporous core contains more than 77% of the spheres volume so that the effective surface area and the adsorption capacity per column are strongly reduced compared to both the completely porous spheres and silica monoliths (Table 6). In this respect, these pellicular particles provide no alternative to the silica-based monoliths with a bimodal pore size distribution.

The bimodal pore size distribution of silica-based monoliths with large macropores and a thin, highly porous (but pressure-stable) skeleton, is the basis for the unique combination of high bed permeability, short diffusion path lengths and high adsorption capacity which cannot be achieved in a fixed bed of any diffusive particle type. Since, up to date, only silica-based monoliths show a distinct bimodal pore

Table 6
Hydrodynamic and adsorption properties of selected porous media

Fixed bed	$\mathscr{L}_{flow}$ (μm)	$\mathscr{L}_{stag}$ (μm)	$\mathscr{R}_{HP}$ liquid hold-up	A_{sp} (m^2/g)	A_{rel} (m^2/ml)	q_{max} (mg/ml)
Silica monolith	11.0	1.0	0.09	91	39	25.7
Pellicular particle	11.0	0.45	0.09	13	14	9.1
Porous spheres B	7.2	3.6	0.5	161	65	40.4

size distribution as a result of their two-step manufacturing process, these columns are clearly favored for use in chromatographic applications especially in those for which the combination of a high bed permeability, short diffusion pathlengths and high surface area is stringently needed like in high-throughput routine analysis, process-scale chromatography using, e.g., simulated moving bed technology, and for determination of compounds in complex mixtures by liquid chromatography on-line coupled to mass spectrometry.

On the other hand, organic polymer monoliths which are characterized by monomodal pore size distributions due to their one-step polymerization process, have been designed for purification processes of biomacromolecules by gradient elution. Since the monomodal pore size distribution provides, for sufficiently large molecules, almost exclusively flow-through pores leaving diffusion-limited mass transfer on transchannel length-scale, the transport of these molecules in polymer monoliths can be considered as being convection-dominated in the pore space available for the analyte. This certainly results in a reduced axial dispersion compared to the high surface area monoliths like the bimodal silica structures. Thus, the hydrodynamic behavior in organic polymer monoliths more resembles that in beds of nonporous spheres. However, the slight, but yet finite porosity of the skeleton, as seen from porosity data and the broad pore size distribution (cf. Fig. 2) suggests that organic polymer monoliths are not completely nonporous and that their skeleton provides, even for molecules of BSA size, accessible pores with a stagnant mobile phase.

5. Nomenclature

A_{spec} specific surface area of the porous medium (m^2/g)
A_{rel} column volume-weighted surface area of porous medium (m^2/ml)
c_{Feed} feed concentration [52] (g/l)
d_{macro} macro or flow-through pore diameter (μm)
d_p average particle diameter (μm)
$\mathscr{D}$ dimensionless dispersivity, Eq. (6)
D_{ax} effective axial dispersion coefficient (m^2/s)
D_m molecular diffusion coefficient (m^2/s)
D_{stag} effective diffusion coefficient in stagnant mobile phase, $D_{stag} = \varepsilon_{intra} K_p D_m / \tau_{intra}$ (m^2/s)
$\bar{d}_{p,2}$ surface area-averaged particle diameter, $\bar{d}_{p,2} = \Sigma\, d_{n,i}^3 n_i / \Sigma d_{n,i}^2 n_i$ (μm)
$\mathscr{F}$ Darcy–Weißbach friction factor
H theoretical plate height (m)
K bed permeability (m^2)
K_p hindrance parameter for pore level diffusion [86]
$\mathscr{L}_{stag}$ characteristic length for liquid hold-up in porous medium
$\mathscr{L}_{disp}$ characteristic length for axial dispersion
$\mathscr{L}_{flow}$ characteristic length for hydraulic permeability
L_{bed} length of packed bed (m)
ΔP pressure drop along column (Pa)
Pe Peclet number
q_i parameter(s) of particle size distribution
q_{area} stationary phase surface concentration (mg/m^2)
q_{max} maximum (monolayer) adsorption capacity (mg/ml)
q_{col} column volume-weighted concentration (mg/ml)
q_{sp} solid-phase concentration (g/l)
Re Reynolds number
$\mathscr{R}_{HP}$ hydrodynamic performance ratio, Eq. (8)
R_G radius of gyration (nm)

$t_{el,i}$ tracer residence time on column (s)
u_{sol} average linear velocity of solute band, $u_{sol} = u_{sf}/\varepsilon_{eff,i}$ (m/s)
u_{av} average mobile phase velocity, $u_{av} = u_{sf}/\varepsilon_{total}$ (m/s)
u_{sf} mobile phase superficial velocity (volumetric flow-rate divided by the column cross sectional area) (m/s)
V_{bed} fixed bed volume (m^3)
V_{extra} extra-column volume (m^3)
$V_{el,i}$ elution volume of solute (m^3)
$\dot{V}$ volumetric flow-rate of the mobile phase (m^3/s)
$\bar{x}$ characteristic radial length scale (m)
σ_L^2 length-scale based variance of a solute band (m^2)
σ_t^2 time-scale based variance of solute band (detector signal) (s^2)
ρ volumetric density of the mobile phase (kg/m^3)
ρ_{bed} volumetric density of fixed bed (kg/m^3)
ε_{total} total porosity of fixed bed (mobile phase volume divided by the column volume)
ε_{inter} interstitial porosity (interstitial void volume—interparticle or interskeleton—divided by column volume) [47]
ε_{intra} porosity of support structure (intraparticle or intraskeleton mobile phase volume divided by the particle or skeleton volume) [47]
$\varepsilon_{eff,i}$ effective bed porosity for analyte i (column residence time divided by the column volume)
τ_{intra} intraparticle or intraskeleton tortuosity factor, $\tau_{intra} = \varepsilon_{intra} + 1.5(1 - \varepsilon_{intra})$ [85]
τ_{bed} bed tortuosity [8,64]
Φ phase ratio (solid-phase volume divided by the liquid phase volume), $\Phi = (1 - \varepsilon_{total})/\varepsilon_{total}$
η dynamic viscosity of the mobile phase (Pa s)
ν kinematic mobile phase viscosity (m^2/s)
ψ_i particle shape distribution parameter(s)
$\Theta_{m,b,h}$ coefficients for mechanical, boundary-layer and hold-up dispersion [63]

Acknowledgements

We are grateful to Dieter Lubda from Merck (Darmstadt, Germany) for the kind donation of the silica-based monoliths and the gift of the particulate media, as well as for his support in providing physical data of the stationary phase materials. We also thank Dr. Gerard Rozing from Agilent Technologies (Waldbronn, Germany) for the donation of HPLC columns. This work was supported by the Deutsche Forschungsgemeinschaft (DFG) under grant SE 586/7-1.

References

[1] R.M. Heck, R.J. Farrauto, Catalytic Air Pollution Control: Commercial Technology, Wiley, New York, 1995.
[2] R.A. Dunbar, J.D. Jordan, F.V. Bright, Anal. Chem. 68 (1996) 604.
[3] F. Kapteijn, J.J. Heiszwolf, T.A. Nijhuis, J.A. Moulijn, CatTech 3 (1999) 24.
[4] A. Kirschning, C. Altwicker, G. Dräger, J. Harders, N. Hoffmann, U. Hoffmann, H. Schönfeld, W. Solodenko, U. Kunz, Angew. Chem. Int. Ed. Engl. 40 (2001) 3995.
[5] F. Svec, J.M.J. Fréchet, Ind. Eng. Chem. Res. 38 (1999) 34.
[6] N. Tanaka, H. Kobayashi, K. Nakanishi, H. Minakuchi, N. Ishizuka, Anal. Chem. 73 (2001) 420A.
[7] D. Josic, A. Buchacher, J. Biochem. Biophys. Methods 49 (2001) 153.
[8] J.C. Giddings, Dynamics of Chromatography. Part I: Principles and Theory, Marcel Dekker, New York, 1965.
[9] P.A. Bristow, J.H. Knox, Chromatographia 10 (1977) 279.
[10] R.F. Probstein, Physiochemical Hydrodynamics, Wiley, New York, 1994.
[11] K.K. Unger, Handbuch der HPLC, GIT Verlag, Darmstadt, 1994.
[12] Cs. Horváth, B.A. Preiss, S.R. Lipsky, Anal. Chem. 39 (1967) 1422.
[13] R.N. Kellerey, F.W. Billmeyer, Anal. Chem. 41 (1969) 874.
[14] K.K. Unger, G. Jilge, J.N. Kinkel, M.T.W. Hearn, J. Chromatogr. 359 (1986) 61.
[15] F. Svec, J.M.J. Fréchet, Anal. Chem. 64 (1992) 820.
[16] Q.C. Wang, F. Svec, J.M.J. Fréchet, J. Chromatogr. A 669 (1994) 230.
[17] F. Svec, J.M.J. Fréchet, Science 273 (1996) 205.
[18] E.C. Peters, F. Svec, J.M.J. Fréchet, Chem. Mater. 9 (1997) 1898.
[19] M.B. Tennikov, N.V. Gazdina, T.B. Tennikova, F. Svec, J. Chromatogr. A 798 (1998) 55.
[20] S. Xie, R.W. Allington, F. Svec, J.M.J. Fréchet, J. Chromatogr. A 865 (1999) 169.
[21] H. Minakuchi, K. Nakanishi, N. Soga, N. Tanaka, Anal. Chem. 68 (1996) 3498.
[22] H. Minakuchi, K. Nakanishi, N. Soga, N. Ishizuka, N. Tanaka, J. Chromatogr. A 762 (1997) 135.
[23] K. Nakanishi, H. Minakuchi, N. Soga, N. Tanaka, J. Sol–Gel Sci. Technol. 8 (1997) 547.

[24] N. Ishizuka, H. Minakuchi, K. Nakanishi, N. Soga, N. Tanaka, J. Chromatogr. A 797 (1998) 133.
[25] K. Cabrera, G. Wieland, D. Lubda, K. Nakanishi, N. Soga, H. Minakushi, K.K. Unger, Trends Anal. Chem. 17 (1998) 50.
[26] H. Minakuchi, K. Nakanishi, N. Soga, N. Ishizuka, N. Tanaka, J. Chromatogr. A 797 (1998) 121.
[27] F. Sinner, M.R. Buchmeiser, Macromolecules 33 (2000) 5777.
[28] K. Nakanishi, N. Soga, J. Am. Ceram. Soc. 74 (1991) 2518.
[29] K. Nakanishi, Y. Sagawa, N. Soga, J. Non-Cryst. Solids 134 (1991) 39.
[30] K. Nakanishi, N. Soga, J. Non-Cryst. Solids 139 (1992) 14.
[31] K. Nakanishi, N. Soga, J. Non-Cryst. Solids 139 (1992) 1.
[32] K. Nakanishi, J. Porous Mater. 4 (1997) 67.
[33] I. Mihelic, T. Koloini, A. Podgornik, A. Strancar, J. High Resolut. Chromatogr. 23 (2000) 39.
[34] M. Vodopivec, A. Podgornik, M. Berovic, A. Strancar, J. Chromatogr. Sci. 38 (2000) 489.
[35] D. Josic, A. Strancar, Ind. Eng. Chem. Res. 38 (1999) 333.
[36] N. Tanaka, H. Nagayama, H. Kobayashi, T. Ikegami, K. Hosoya, N. Ishizuka, H. Minakuchi, K. Nakanishi, K. Cabrera, D. Lubda, J. High Resolut. Chromatogr. 23 (2000) 111.
[37] K. Cabrera, D. Lubda, H.-M. Eggenweiler, H. Minakuchi, K. Nakanishi, J. High Resolut. Chromatogr. 23 (2000) 93.
[38] D. Lubda, K. Cabrera, W. Kraas, C. Schäfer, D. Cunningham, LC–GC Int. 14 (2001) 730.
[39] A. Podgornik, M. Barut, A. Strancar, D. Josic, T. Koloini, Anal. Chem. 72 (2000) 5693.
[40] C. Yu, M.H. Davey, F. Svec, J.M.J. Fréchet, Anal. Chem. 73 (2001) 5088.
[41] D.S. Petersen, T. Rohr, F. Svec, J.M.J. Fréchet, Anal. Chem. 74 (2002) 4081.
[42] Q.S. Yuan, A. Rosenfeld, T.W. Root, D.J. Klingenberg, E.N. Lightfoot, J. Chromatogr. A 831 (1999) 149.
[43] J. Bear, Dynamics of Fluids in Porous Media, Dover Publications, New York, 1988.
[44] S. Ergun, Chem. Eng. Sci. 48 (1952) 89.
[45] K.E.B. Andersson, Chem. Eng. Sci. 15 (1961) 276.
[46] I.F. Macdonald, M.S. El-Sayed, K. Mow, F.A.L. Dullien, Ind. Eng. Chem. Fundam. 18 (1979) 199.
[47] F.C. Leinweber, D. Lubda, K. Cabrera, U. Tallarek, Anal. Chem. 74 (2002) 2470.
[48] U. Tallarek, F.C. Leinweber, A. Seidel-Morgenstern, Chem. Eng. Technol. 25 (2002) 1177.
[49] J.P. Foley, J.G. Dorsey, Anal. Chem. 55 (1983) 730.
[50] M.S. Jeansone, J.P. Foley, J. Chromatogr. Sci. 29 (1991) 258.
[51] V.B.D. Marco, G.G. Bombi, J. Chromatogr. A 931 (2001) 1.
[52] R.M. Nicoud, A. Seidel-Morgenstern, Isolation Purif. 2 (1996) 165.
[53] P.C. Carman, Trans. Inst. Chem. Eng. 15 (1937) 150.
[54] A.R. Gupte, Ph.D. dissertation, Fakultät für Chemieingenieurwesen, Technische Hochschule Karlsruhe, Karlsruhe, 1970.
[55] H. Rumpf, A.R. Gupte, Chem.-Ing.-Tech. 43 (1971) 367.
[56] J.I. Liao, N. Chen, C. Ericson, S. Hjertén, Anal. Chem. 68 (1996) 3468.
[57] B. Mayr, R. Tessadri, E. Post, M.R. Buchmeiser, Anal. Chem. 73 (2001) 4071.
[58] A. Premstaller, H. Oberacher, C.G. Huber, Anal. Chem. 73 (2001) 4386.
[59] Q. Luo, H. Zou, X. Xiao, Z. Guo, L. Kong, X. Mao, J. Chromatogr. A 926 (2001) 255.
[60] R. Hahn, A. Jungbauer, Anal. Chem. 72 (2000) 4853.
[61] S. Ghose, S.M. Cramer, J. Chromatogr. A 928 (2001) 13.
[62] J.J. van Deemter, F.J. Zuiderweg, A. Klinkenberg, Chem. Eng. Sci. 5 (1956) 271.
[63] D.L. Koch, J.F. Brady, J. Fluid Mech. 154 (1985) 399.
[64] D. Kandhai, D. Hlushkou, A.G. Hoekstra, P.M.A. Sloot, H. Van As, U. Tallarek, Phys. Rev. Lett. 88 (2002) art. no. 234501.
[65] S.G. Weber, P.W. Carr, in: P.R. Brown, R.A. Hartwick (Eds.), High Performance Liquid Chromatography, Wiley, New York, 1989, Chapter 1.
[66] D.R. Lide, CRC Handbook of Chemistry and Physics, CRC Press, Boca Raton, 1997.
[67] A.E. Kamholz, E.A. Schilling, P. Yager, Biophys. J. 80 (2001) 1967.
[68] H. Olesen, J. Rehfeld, B.L. Hom, E. Hippe, Biochim. Biophys. Acta 194 (1969) 67.
[69] M.E. Young, P.A. Carroad, R.L. Bell, Biotechnol. Bioeng. 22 (1980) 947.
[70] M.T. Tyn, T.W. Gusek, Biotechnol. Bioeng. 35 (1990) 327.
[71] G. Guiochon, S. Golshan-Shirazi, A.M. Katti, Fundamentals of Preparative and Nonlinear Chromatography, Academic Press, Boston, 1994.
[72] T. Fornstedt, G. Guiochon, Anal. Chem. 73 (2001) 608A.
[73] D.M. Ruthven, Principles of Adsorption and Adsorption Processes, Wiley, New York, 1984.
[74] E. Glückauf, Nature 156 (1945) 748.
[75] G. Schay, G. Székely, Acta Chim. Acad. Sci. Hung. 5 (1954) 167.
[76] D.H. James, C.S.G. Phillips, J. Chem. Soc (1954) 1066.
[77] J.M. Jacobson, J.H. Frenz, Cs. Horváth, J. Chromatogr. 316 (1984) 53.
[78] J.M. Jacobson, J.H. Frenz, Cs. Horváth, Ind. Eng. Chem. Res. 26 (1987) 43.
[79] H.S. Carslaw, J.C. Jaeger, Conduction of Heat in Solids, Oxford University Press, Oxford, 1959.
[80] J. Crank, The Mathematics of Diffusion, Oxford University Press, Oxford, 1975.
[81] G. Greco, G. Iorio, G. Tola, S.P. Waldram, Trans. Inst. Chem. Eng. 53 (1975) 55.
[82] E.D. Heyse, D.J. Mika, T.P. deVenoge, D.L. Couliette, A. McGowin, Environ. Toxicol. Chem. 18 (1999) 1964.
[83] Z.P. Lu, M.M. Dias, J.C.B. Lopes, A.E. Rodrigues, Ind. Eng. Chem. Res. 32 (1993) 1839.
[84] A.E. Rodrigues, J.C.B. Lopes, M.M. Dias, G. Carta, Sep. Technol. 2 (1992) 208.
[85] M. Suzuki, J.M. Smith, Chem. Eng. J. 3 (1972) 256.
[86] H. Brenner, L.J. Gaydos, J. Colloid Interface Sci. 58 (1977) 312.